# Electronic Supplementary Information

## Constructing carboxyl-rich angstrom-level trap in metal-organic framework for selective capture of lithium

Xinxin Gao,[a] Rui Ding,[a] Hongliang Huang,*[c] Baosheng Liu,*[b] and Xudong Zhao*[a]

[a]College of Chemical Engineering and Technology, Taiyuan University of Science and Technology, Taiyuan 030024, China.

[b]College of Materials Science and Engineering, Taiyuan University of Science and Technology, Taiyuan 030024, China.

[c]State Key Laboratory of Separation Membranes and Membrane Processes, School of Chemical Engineering and Technology, Tiangong University, Tianjin 300387, China.

## Experimental section

### Chemicals

1,2,4,5-benzenetetracarboxylic acid ($H_2$ linker, 98%), benzenehexacarboxylic acid ($H_4$ linker, > 98.0%), zirconium oxychloride octahydrate ($ZrOCl_2 \cdot 8H_2O$, 98.0%), acetic acid (AA, 99 %), sodium chloride (NaCl, >99.5%), potassium chloride (KCl, ≥ 99.5%), anhydrous calcium chloride ($CaCl_2$, > 96.0%), anhydrous magnesium chloride ($MgCl_2$, 99%+), and anhydrous lithium chloride (LiCl, 99%) are purchased from HWRK Chem. The deionized water was made by our laboratory.

### Synthesis

***Synthesis of UiO-66-$H_2$***. In a 50 mL round-bottom flask, $ZrOCl_2 \cdot 8H_2O$ (4 mmol, 1.288 g) and $H_2$ linker (4 mmol, 1.016 g) were well dissolved in the mixture of water (10 mL) and AA (10 mL). After being stirred for 10 min at room temperature, this system was refluxed at 100 °C for 24 h. The white solid was collected and washed with water and ethanol. Finally, the sample was dried at 100 °C for 24 h.

***Synthesis of UiO-66-$H_4$***. The preparation of this material is consistent with that of UiO-66-$H_2$, except for the substitution of $H_2$ linker by equimolar $H_4$ linker.

***Synthesis of UiO-66-$H_2$/$H_4$***. In a 50 mL round-bottom flask, $ZrOCl_2 \cdot 8H_2O$ (4 mmol, 1.288 g) and organic liners (4 mmol) with different $H_2$/$H_4$ molar ratios (3:1, 2:2, and 1:3) were added. The following procedures are similar to that of UiO-66-$H_2$. The samples were named as UiO-66-$H_2$/$H_4$-a,b,c according to the $H_2$/$H_4$ ratios of 3:1, 2:2 and 1:3, respectively.

### Characterization methods

The X-ray diffraction (XRD) patterns of samples were obtained using an X-ray diffractometer (Panalytical Empyrean). The specific surface area and pore characteristics were determined by $N_2$ adsorption and desorption method at 77 K on an Automatic surface and porosity analyzer (Micromeritics ASAP 2046). Zeta potentials were measured on the Nano particle size and Zeta potential analyzer (Malvern Nano ZS90). Elemental analysis (EA) of samples was determined on an organic element analyzer (Elementar UNICUBE). X-ray photoelectron spectroscopy (XPS) data was performed on an Axis Supra X-ray photoelectron spectroscope.

TEM images were obtained on an F-200 transmission electron microscope. $^{13}C$ nuclear magnetic resonance (NMR) patterns were measured on a JNM-ECZ400S/L1 spectrometer. The sample was prepared via dissolving MOF sample (40 mg) into a mixture of $H_2SO_4$ (0.5 mL) and DMSO-$d_6$ (0.6 mL).

**Theoretical calculation methods**

DFT calculations were carried out using the CP2K code.[1] All calculations employed mixed Gaussian and plane-wave basis sets. Core electrons were represented with norm-conserving Goedecker-Teter-Hutter pseudopotentials,[2-4] and the valence electron wavefunction was expanded in a double-zeta basis set with polarization functions along with an auxiliary plane-wave basis set with an energy cutoff of 400 eV.[5] The generalized gradient approximation exchange-correlation functional of Perdew, Burke, and Enzerhof (PBE) was used.[6] Each configuration was optimized with the Broyden-Fletcher-Goldfarb-Shanno (BGFS) algorithm with SCF convergence criteria of $1.0\times10^{-8}$ au. To compensate for the long-range van der Waals dispersion interaction between the adsorbate and the zeolite, the DFT-D3 scheme with an empirical damped potential term was added to the energies obtained from exchange-correlation functional in the calculations.[7] The interaction energy of $Li^+$ ion in the MOF was calculated by the following Eq. (1):

$$\Delta E = E(MOF - Li^+) + E(H^+) - E(MOF) - E(Li^+) \qquad (1)$$

where $E(MOF\text{-}Li^+)$ is the total energy of the MOF with the binding $Li^+$ ion; $E(MOF)$ is the total energy of the MOF; $E(Li^+)$ and $E(H^+)$ are the energies of the $Li^+$ ion and hydrogen ion.

**Adsorption experiments**

In a 20 mL glass vial, the solid adsorbent (5 mg) was added in the aqueous solution (10 mL), and the resulting solid-liquid suspension was stirred at 303 K in a constant temperature shaker. After that, the clear filtrate was collected *via* a microfiltration membrane and further used to determine the concentrations of the metal ions via an inductively coupled plasma optical emission spectrometer (ICP-OES, Avio 200, PekinElmer). The adsorption amount ($Q$, mg $g^{-1}$) was calculated by the following equation:

$$Q = \frac{(C_0 - C_e) \times V}{m} \quad (2)$$

where $C_0$ (mg $L^{-1}$) and $C_e$ (mg $L^{-1}$) are the initial and final concentrations of the metal ions respectively, $V$ (L) is the volume of the solution and $m$ (g) is the adsorbent mass.

The experimental conditions for binary-component adsorption are similar to that. The distribution coefficient ($K_d$) and selectivity factor ($\alpha$) were calculated to determine the adsorption selectivity by the Eqs. (3, 4):

$$K_d = \frac{Q}{C_e} \quad (3)$$

$$\alpha = \frac{K_d^{Li}}{K_d^{M}} \quad (4)$$

**Regeneration method**

The $Li^+$-adsorbed sample (50 mg) was immersed in a $HNO_3$ aqueous solution (pH=2.0, 100 mL) for 12 h. The collected sample was washed with deionized water (10 mL). The sample was finally dried at 100 °C for 12 h.

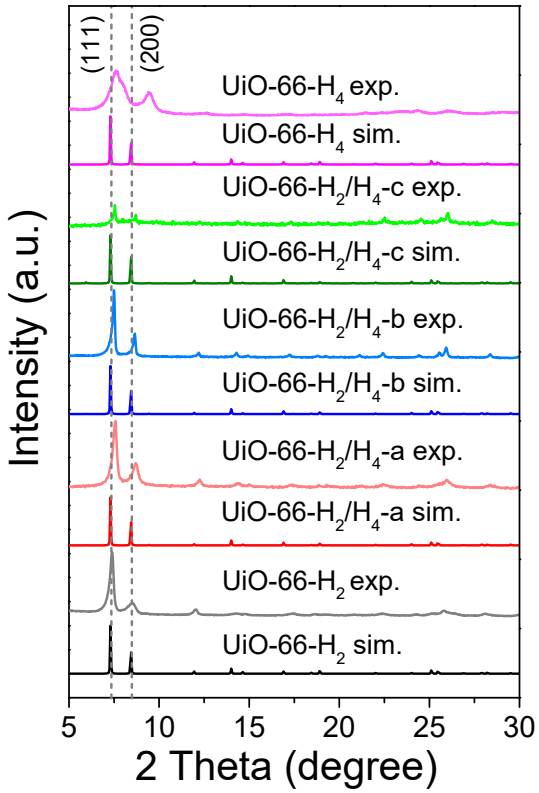


**Fig. S1** The powder and simulated XRD patterns of the MOFs

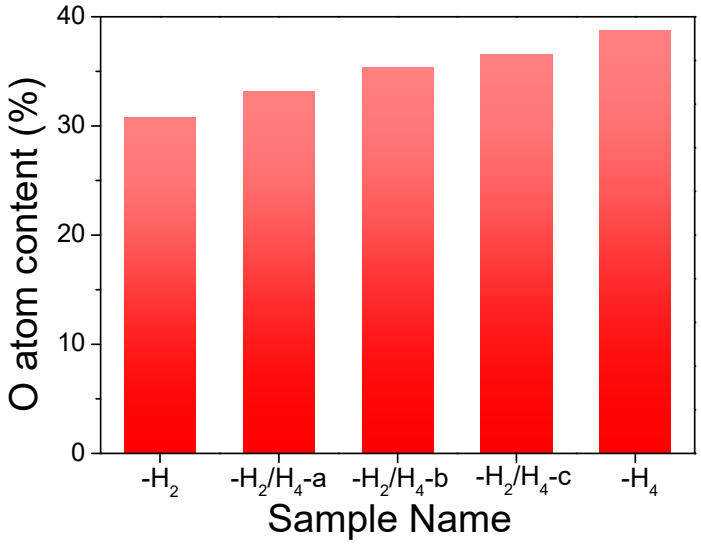


**Fig. S2** The O contents in the samples based on EA results

**Qualitative analysis of $H_2$ linker based on UV method:**

The MOF sample (20 mg) was completely dissolved in a mixed solution of $H_2SO_4$ and DMSO (v/v, 0.5/0.8 mL) under an ultrasonic treatment. The solution was diluted 1000 times and then used to measure the UV curves on an UV-Vis spectrometer (UV-6300).

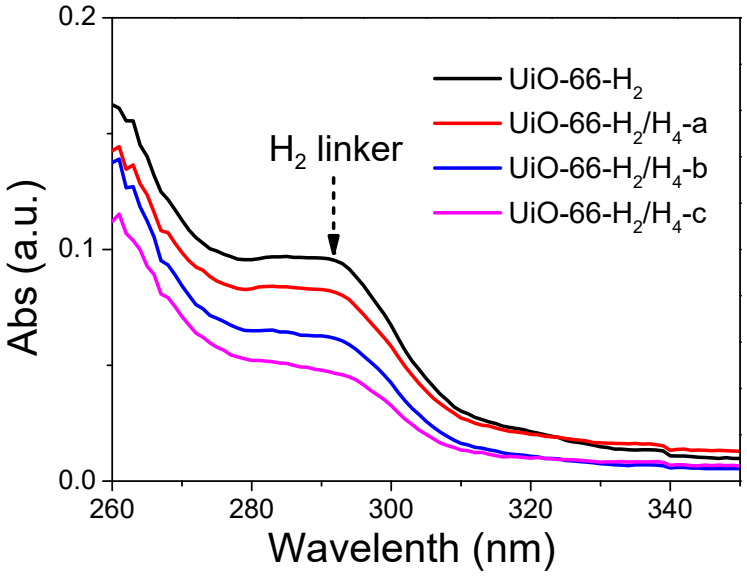


**Fig. S3** The UV curves of the dissolved solution of the MOFs

**Table S1** Pore parameters of the samples

| Sample | $S_{BET}$ ($m^2/g$)[a] | $S_{micro}$ ($m^2/g$)[b] | $V_{total}$ ($cm^3/g$)[c] |
|---|---|---|---|
| UiO-66-$H_2$ | 630.18 | 542.81 | 0.5458 |
| UiO-66-$H_2$/$H_4$-a | 492.78 | 390.67 | 0.5808 |
| UiO-66-$H_2$/$H_4$-b | 326.11 | 275.84 | 0.2653 |
| UiO-66-$H_2$/$H_4$-c | 214.72 | 159.99 | 0.2098 |
| UiO-66-$H_4$ | 137.11 | 7.72 | 0.8037 |

[a]$S_{BET}$ is the Brunauer-Emmett-Teller specific surface area;

[b]$S_{micro}$ is the *t*-plot micropore surface area;

[c]$V_{total}$ is the total specific pore volume determined based on the value at $P/P_0$=0.99 in adsorption curve;

The formation of defects was confirmed by TGA result, which is considered a feasible method to quantify defects. The curve can be featured by a three-stage weight loss process: (i) the volatilization of the solvents at T < 100 °C; (ii) the removal of free acids, coordinated acetic acids, and dehydroxylation of the Zr6 cluster [$Zr_6O_4(OH)_4 \rightarrow Zr_6O_6 + 2H_2O$] at 100 °C < T < 270 °C, where the formula of the sample is considered as $Zr_6O_6(BHC)_n$; (iii) the decomposition of the framework to form $ZrO_2$ at 270 °C < T < 700 °C, where the BHC ligands were completely combusted. Based on the mass conservation of Zr content, the value of n can be calculated according to the following equation:

$$\frac{35.6\%}{M[ZrO2]} = \frac{(41.7 + 35.6)\%}{M[Zr6O6(BHC)n]} \times 6$$

The value of n was found to be obviously less than the standard value of 6.0. This confirms the absence of parts of the ligands and thereby the formation of the defects.

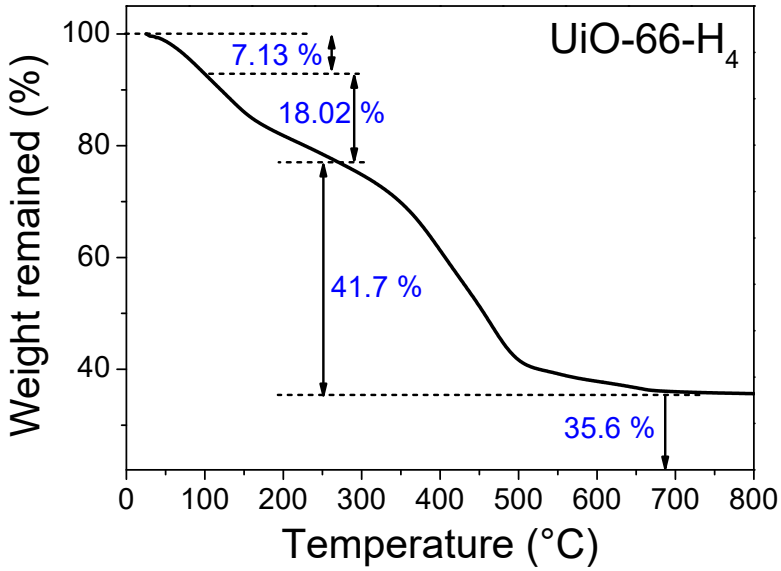


**Fig. S4** TGA curve of UiO-66-$H_4$ under air

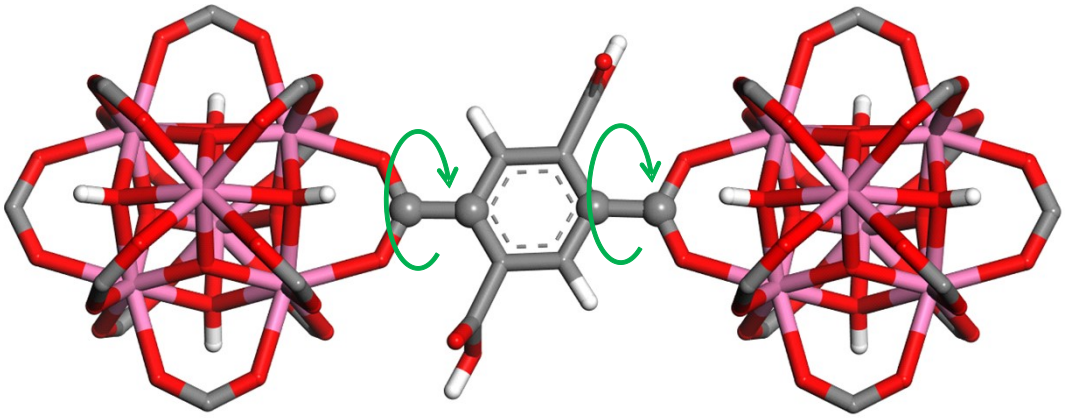

**Fig. S5** The schematic image for the rotatable C-C bonds in the UiO-66 class

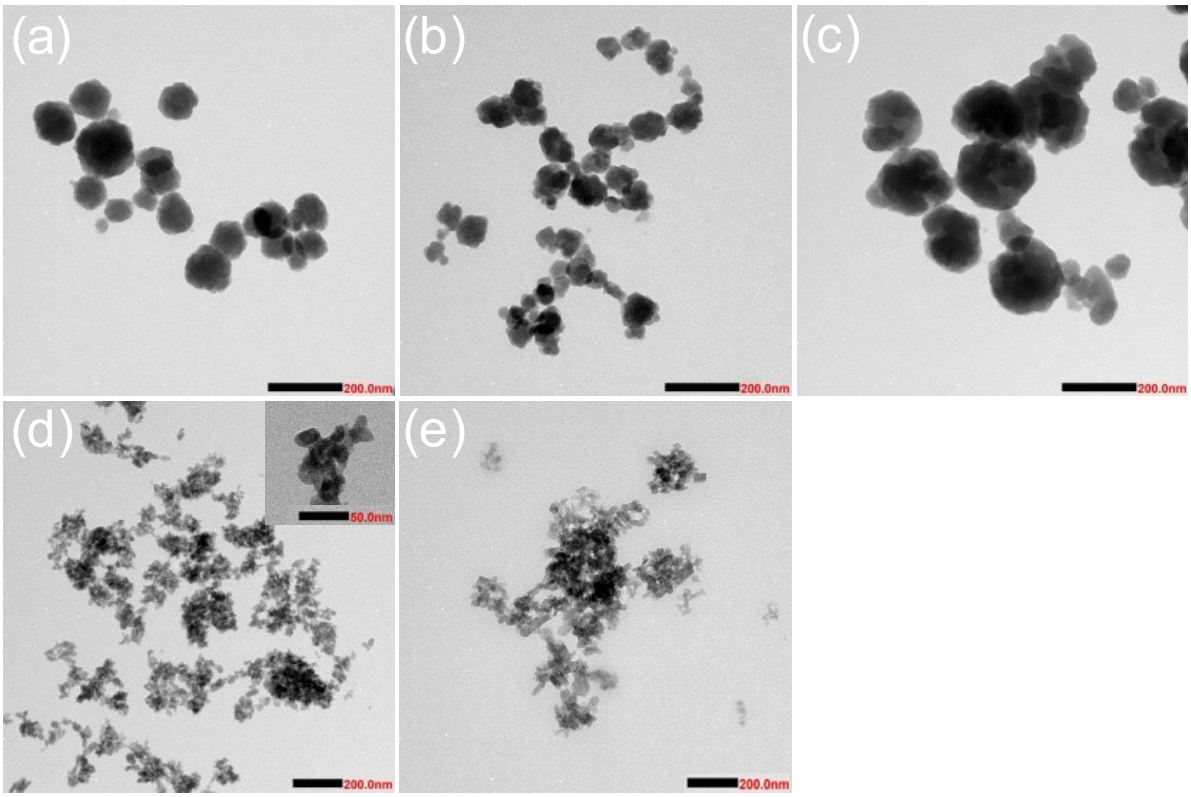


**Fig. S6** The TEM images for the samples: (a) UiO-66-$H_2$, (b) UiO-66-$H_2$/$H_4$-a, (c) UiO-66-$H_2$/$H_4$-b, (d) UiO-66-$H_2$/$H_4$-c, and (e) UiO-66-$H_4$

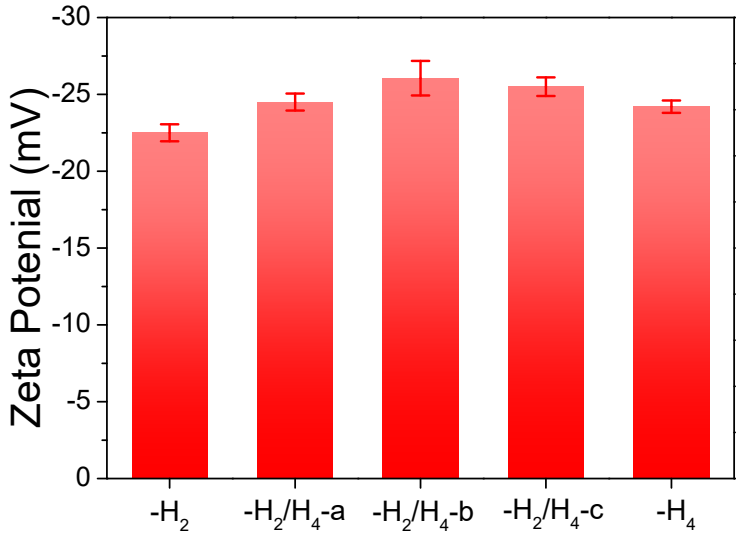


**Fig. S7** The zeta potentials of the samples at pH of 6.0 (close to the natural pH of $Li^+$-containing solution)

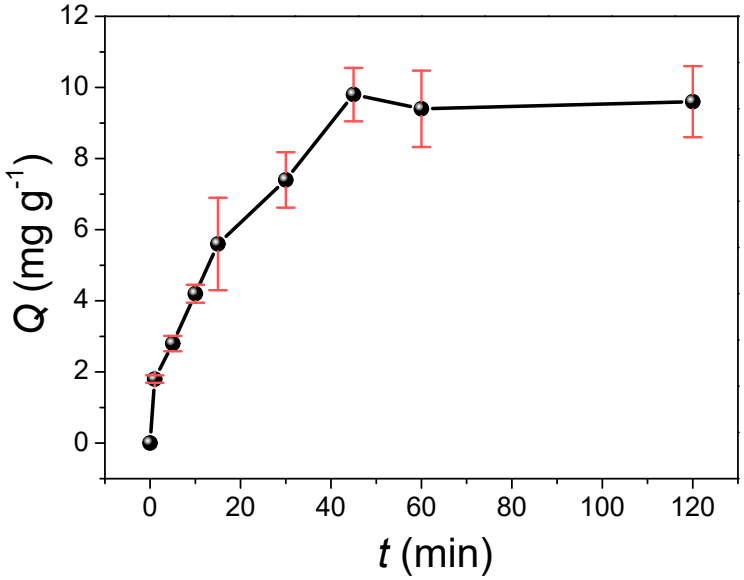


**Fig. S8** The adsorption amount of $Li^+$ ion in UiO-66-$H_2$/$H_4$-b at various time

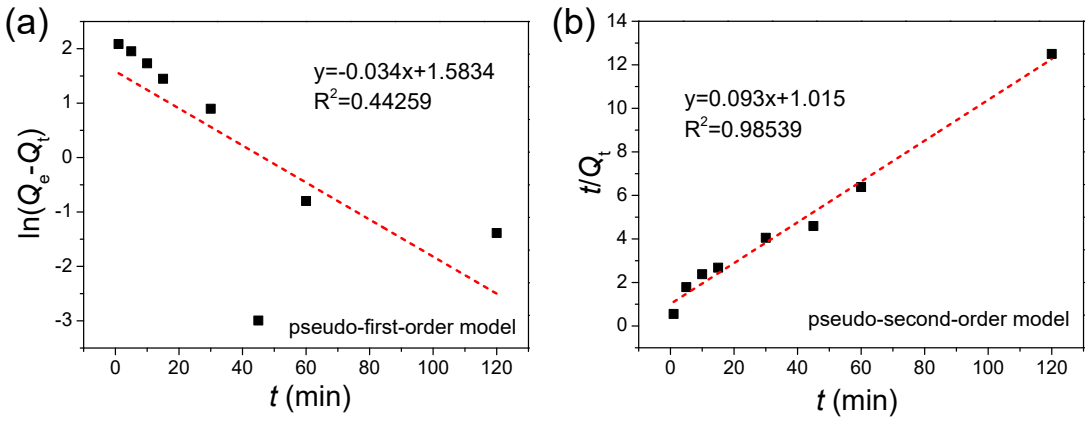


**Fig. S9** (a) Pseudo-first-order kinetic fitting curves and (b) pseudo-second-order kinetic fitting curves of $Li^+$ ion adsorption in UiO-66-$H_2$/$H_4$-b

**Table S2** Kinetic fitting parameters of $Li^+$ ion adsorption in UiO-66-$H_2$/$H_4$-b

| $Q_{e,exp}$ (mg $g^{-1}$) | pseudo-first-order model | | | pseudo-second-order model | | |
|---|---|---|---|---|---|---|
| | $Q_{e,cal}$ (mg $g^{-1}$) | $k_1$ ($min^{-1}$) | $R^2$ | $Q_{e,cal}$ (mg $g^{-1}$) | $k_2$ (g $min^{-1}$ $mg^{-1}$) | $R^2$ |
| 9.85 | 4.7 | 0.034 | 0.4426 | 10.75 | 0.0085 | 0.9854 |

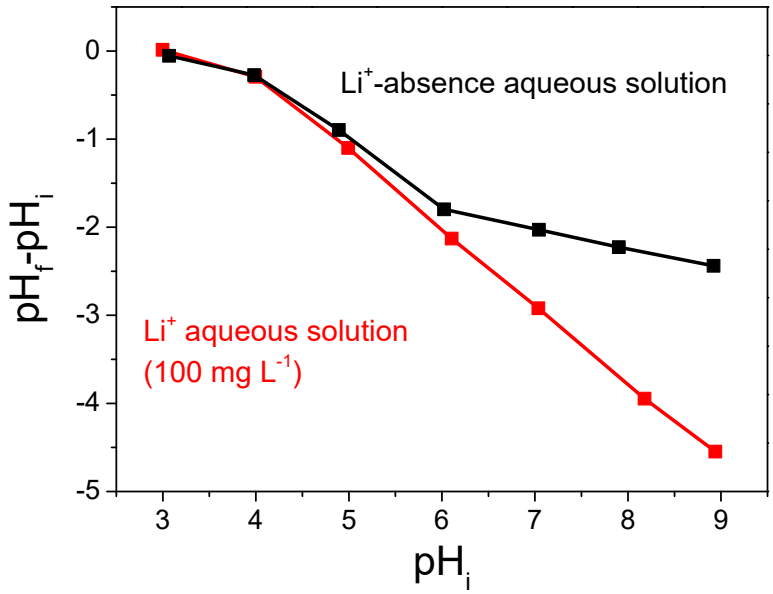


**Fig. S10** The pH change of the solutions after the addition of UiO-66-$H_2$/$H_4$-b sample ($pH_i$, the initial pH; $pH_f$, the final pH).

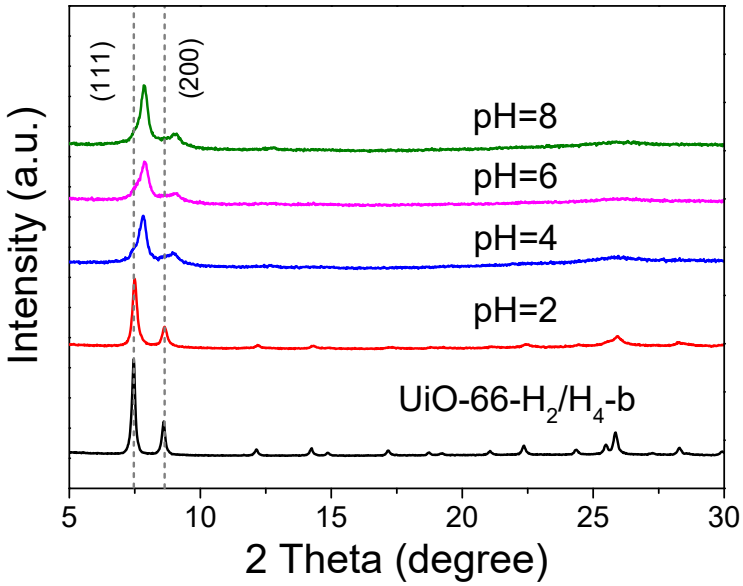


**Fig. S11** Powder XRD patterns of the sample after being immersed in the aqueous solutions for 12 h

At pH=2.0, the main diffraction peaks (111) and (200) almost remain unchanged. For higher pH of 4.0-8.0, the diffraction peaks are slightly shifted. This skewing may be attributed to the following reasons: (a) First, it should be noted that the density of –COOH groups is very high in a local region. These free –COOH groups with close distance are easily to form associated –COOH groups, based on H-bond interaction. (b) At pH=4.0-8.0, the formation of associated –COOH groups induces the distortion of the MOF framework and thereby the shift of XRD diffraction peaks. (c) At the acidic pH of 2.0, the excessive $H^+$ ions lead to the protonization of the O atoms in -COOH groups. As a result, the atoms that can form hydrogen bonds are reduced. Thus, the associated phenomenon of free -COOH groups may be limited.

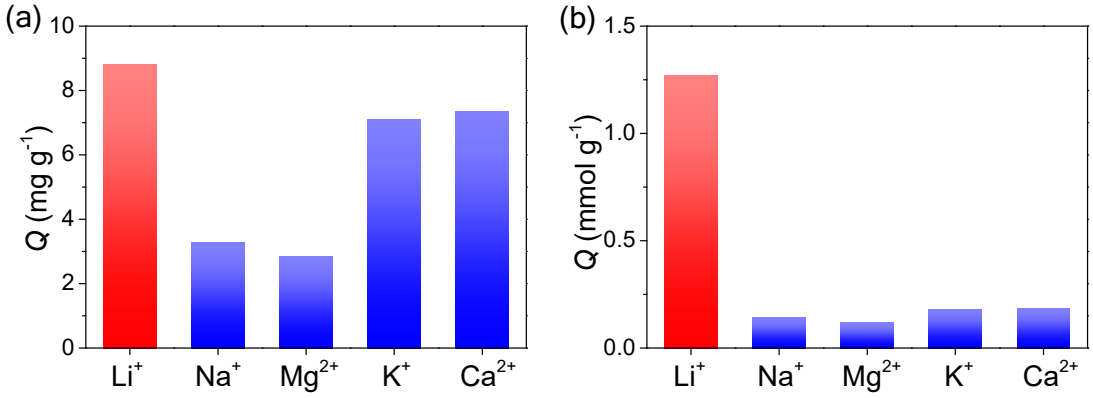


**Fig. S12** Adsorption amounts of UiO-66-$H_2$/$H_4$-b for various ions at $C_0$ of 100 mg $L^{-1}$: (a) Mass adsorption amount and (b) molar adsorption amount

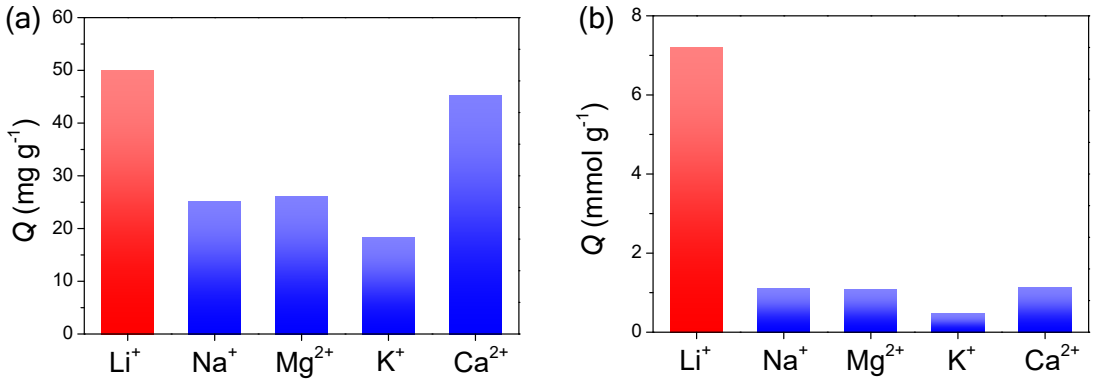


**Fig. S13** Adsorption amounts of UiO-66-$H_2$/$H_4$-b for various ions at $C_0$ of 1000 mg $L^{-1}$: (a) Mass adsorption amount and (b) molar adsorption amount

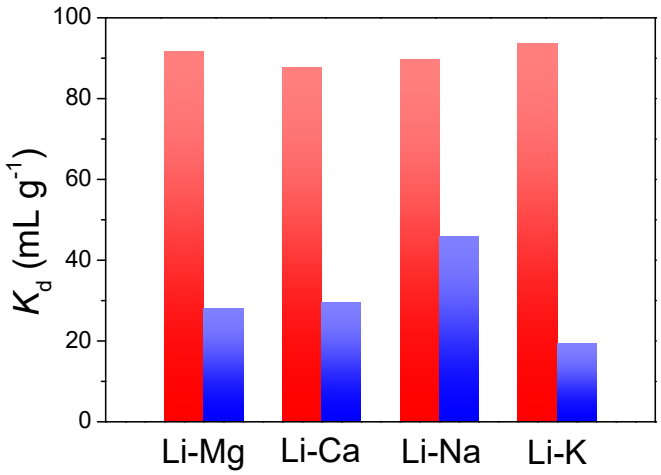


**Fig. S14** The partition coefficient $K_d$ for the ions in the binary-component solutions (the red is for $Li^+$ and the blue is for $Mg^{2+}$, $Ca^{2+}$, $Na^+$ and $K^+$)

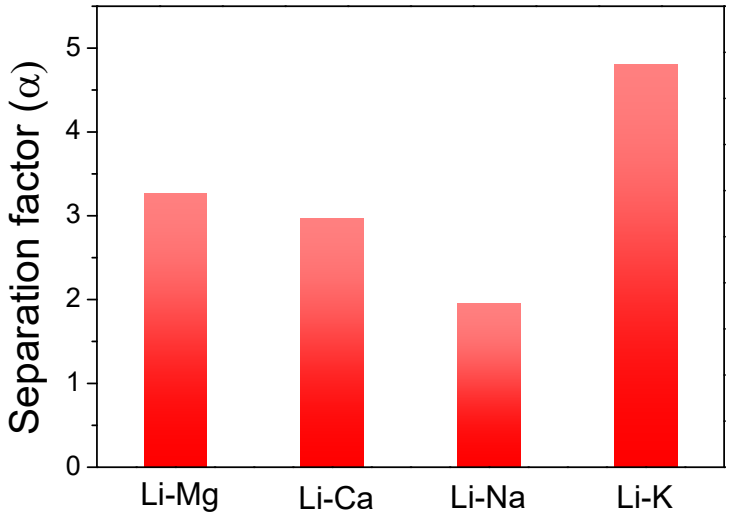


**Fig. S15** The separation factors (α) for $Li^+$ ion over other ions

**Table S3** The elements compositions of surface brine in Xitai Salt Lake[8]

| Ion | $Cl^-$ | $SO_4^{2-}$ | $K^+$ | $Na^+$ | $Ca^{2+}$ | $Mg^{2+}$ | $Li^+$ |
|---|---|---|---|---|---|---|---|
| $C_{real}$ (mg/L)[8] | 8.72 | 1.61 | 0.28 | 5.05 | 0.15 | 0.56 | 8.72 |
| $C_{simu}$ (mg/L) | 4.47 | 3.57 | 0.34 | 9.37 | 0.10 | 0.49 | 8.54 |

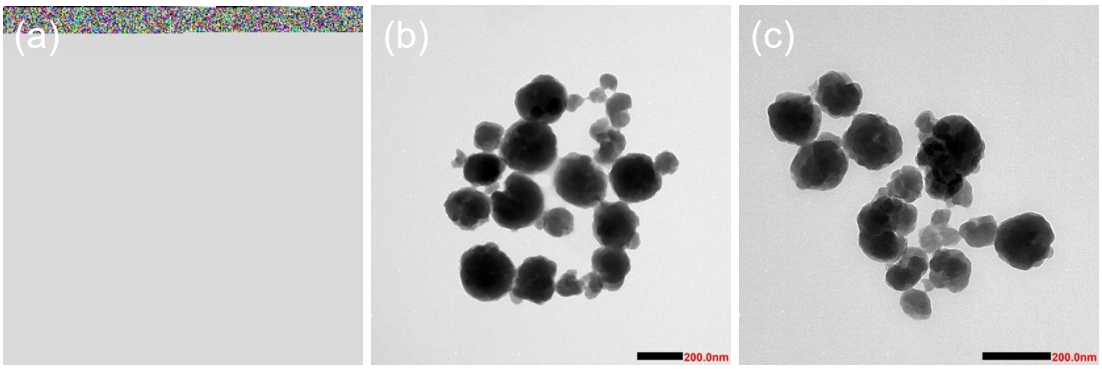


**Fig. S16** TEM images of (a) original UiO-66-$H_2$/$H_4$-b sample, (b) $Li^+$ ion adsorbed sample, and (c) regenerated sample

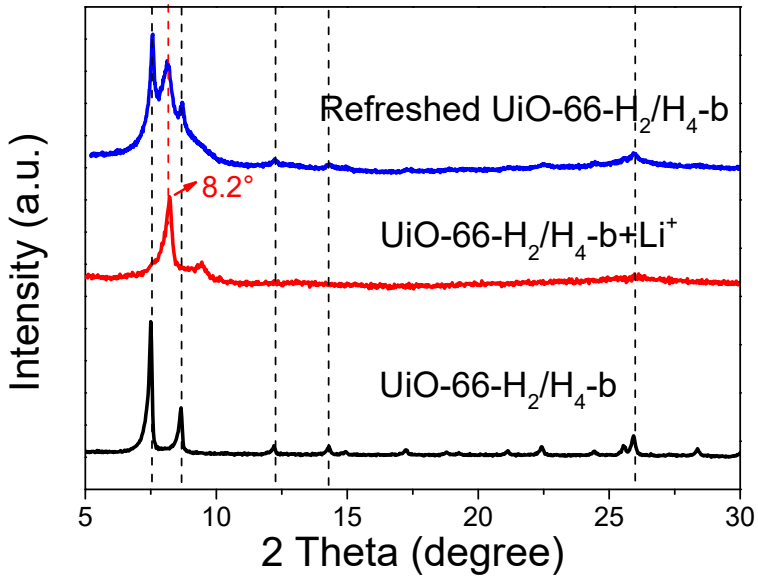


**Fig. S17** Powder XRD patterns of original UiO-66-$H_2$/$H_4$-b sample, $Li^+$ ion adsorbed sample, and the regenerated sample.

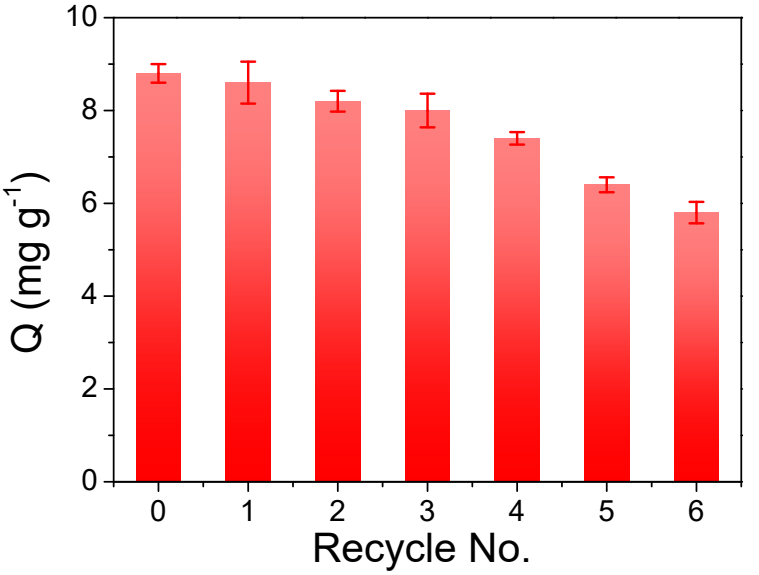


**Fig. S18** The adsorption amount UiO-66-$H_2$/$H_4$-b for $Li^+$ ion after being refreshed (adsorption condition: MOF usage, 0.5 g/L; $C_0$, 100 mg/L; $t$, 12 h; $T$, 303 K; pH, ~6.5)

**Table S4** Comparison of the adsorption capacity of UiO-66-$H_2$/$H_4$-b (6 cycles) with other reported adsorbents

| Sample Name | $Q$ (mg/g) | T (K) | $C_0$ (mg/L) | Ref. |
|---|---|---|---|---|
| $Fe_3O_4$@$SiO_2$@IIP | 4.1 | 298 | ~100 | 9 |
| GLDH | ~5.0 | 288 | 250 | 10 |
| MLDH-1 | 5.83 | 298 | 250 | 11 |
| PDMVBA-MIL-121 | 1.38 | - | 1000 | 12 |
| lithium-aluminum adsorbent | 2.015 | 303 | 1000 | 13 |
| pNCE-MOF-808 | 0.378 | 293 | 3500 | 14 |
| **UiO-66-$H_2$/$H_4$-b (6 cycles)** | 5.8 | 303 | 100 | This work |

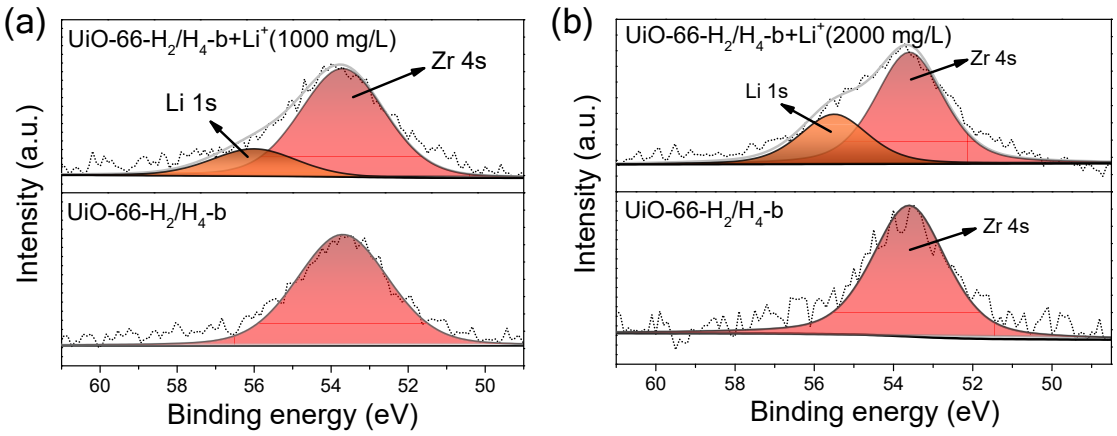


**Fig. S19** The Zr 4s XPS patterns of UiO-66-$H_2$/$H_4$-b before and after $Li^+$ adsorption and its peak splitting results (herein, it is noted that the signs of Li 1s and Zr 4s are overlapped)

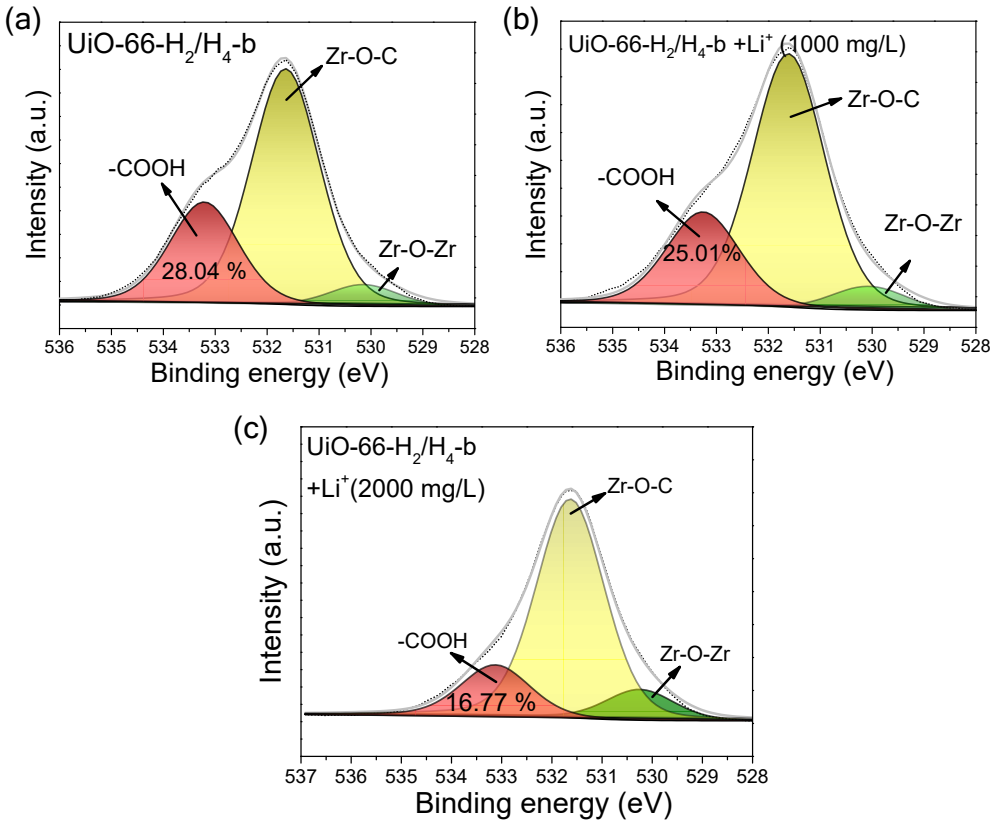


**Fig. S20** The O 1s XPS patterns of (a) pristine UiO-66-$H_2$/$H_4$-b sample, (b) $Li^+$-adsorbed sample (1000 mg $L^{-1}$), and (c) $Li^+$-adsorbed sample (2000 mg $L^{-1}$).

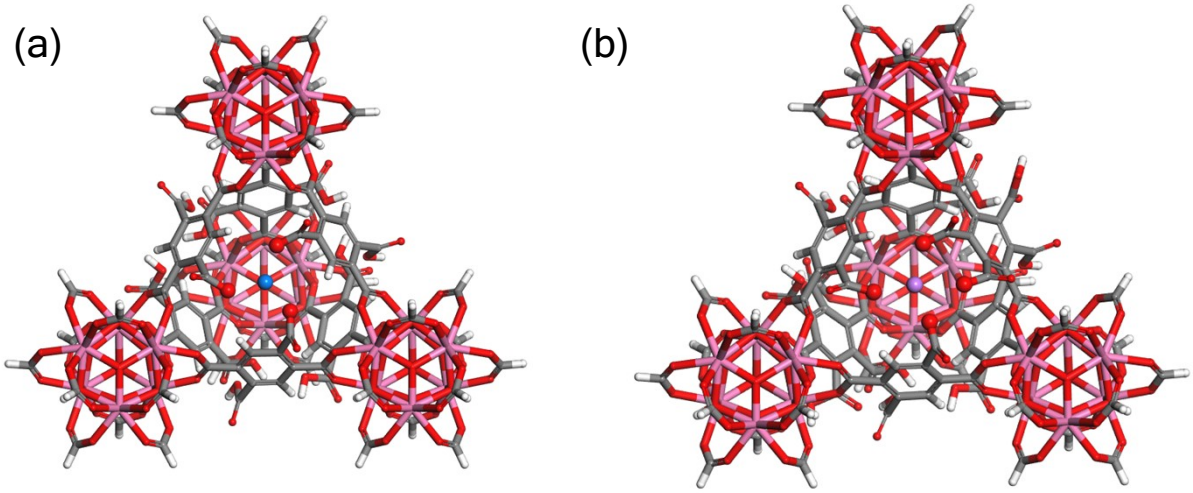


**Fig. S21** The optimized configuration for $Li^+$ adsorption in (a) UiO-66-$H_2$ and (b) UiO-66-$H_2$/$H_4$-b

## References


1. J. VandeVondele, M. Krack, F. Mohamed, M. Parrinello, T. Chassaing, J. Hutter, Quickstep: fast and accurate density functional calculations using a mixed Gaussian and plane waves approach, Comput. Phys. Commun. 2005, 167, 103-128.
2. S. Goedecker, M. Teter, J. Hutter, Separable Dual-space gaussian pseudopotentials, Phys. Rev. B 1996, 54, 1703-1710.
3. C. Hartwigsen, S. Goedecker, J. Hutter, Relativistic separable dual-space gaussian pseudopotentials from H to Rn, Phys. Rev. B 1998, 58, 3641-3662.
4. M. Krack, M. Parrinello, All-electron ab-initio molecular dynamics, Phys. Chem. Chem. Phys. 2000, 2, 2105-2112.
5. J. VandeVondele, J. Hutter, Gaussian basis sets for accurate calculations on molecular systems in gas and condensed phases, J. Chem. Phys. 2007, 127, 114105.
6. J.P. Perdew, K. Burke, M. Ernzerhof, Generalized gradient approximation made simple, Phys. Rev. Lett. 1996, 77, 3865.
7. S. Grimme, J. Antony, S. Ehrlich, H. Krieg, A consistent and accurate ab initio parametrization of density functional dispersion correction (DFT-D) for the 94 elements H-Pu, J. Chem. Phys. 2010, 132, 154104.
8. M.-Y. He, C.-G. Luo, H.-J. Yang, F.-C. Kong, Y.-L. Li, L. Deng, X.-Y. Zhang, K.-Y. Yang, Sources and a proposal for comprehensive exploitation of lithium brine deposits in the Qaidam Basin on the northern Tibetan Plateau, China: Evidence from Li isotopes, Ore. Geo. Rev., 2020, 117, 103277.
9. X. Luo, B. Guo, J. Luo, F. Deng, S. Zhang, S. Luo, J. Crittenden, Recovery of lithium from wastewater using development of Li ion-imprinted polymers, ACS Sustainable Chem. Eng. 2015, 3, 460-467.
10. J. Zhong, S. Lin, J. Yu, Lithium recovery from ultrahigh $Mg^{2+}/Li^{+}$ ratio brine using a novel granulated Li/Al-LDHs adsorbent, Sep. Purif. Technol. 2021, 256, 117780.
11. J. Chen, S. Lin, J. Yu, Quantitative effects of $Fe_3O_4$ nanoparticle content on $Li^{+}$ adsorption and magnetic recovery performances of magnetic lithium-aluminum layered double hydroxides in ultrahigh Mg/Li ratio brines, J. Hazard. Mater., 2020, 388, 122101.
12. R. Ou, H. Zhang, J. Wei, S. Kim, L. Wan, N.S. Nguyen, Y. Hu, X. Zhang, G.P. Simon, H. Wang, Thermoresponsive amphoteric metal-organic frameworks for efficient and reversible adsorption of multiple salts from water, Adv. Mater., 2018, 30, 1802767.
13. H. Jiang, Y. Yang, S. Sun, J. Yu, Adsorption of lithium ions on lithium-aluminum hydroxides: Equilibrium and kinetics, Can. J. Chem. Eng., 2019, 98, 544-555.
14. S. Zhang, R. Ou, H. Ma, J. Lu, M.M. Banaszak Holl, H. Wang, Thermally regenerable metal-organic framework with high monovalent metal ion selectivity, Chem. Eng. J. 2021, 405, 127037.